An Antenna Pattern Correction Algorithm for Conical Scanning Spaceborne Radiometers: The CIMR Case

Alessandro Lapini, Ada Vittoria Bosisio, *Member, IEEE*, Giovanni Macelloni, *Senior Member, IEEE*, and Marco Brogioni, *Member, IEEE*

Abstract—The rapid evolution of the effects observed in various areas of our planet related to climate change poses urgent questions about the knowledge of the state of the polar area and requires satellite acquisitions with fine spatial resolution and high accuracy to develop advanced products. The Copernicus Imaging Microwave Radiometer (CIMR) mission, based on a multifrequency microwave radiometer and designed to observe the ocean, sea ice, and Arctic environment, requires brightness temperature measurements with a total absolute uncertainty of 0.5 K and a spatial resolution of 5 km. This constraint demands very large reflectors with a gain value of tens of decibels. Mechanical constraints will be attained by using a mesh reflector, which guarantees the required resolution but with the drawback of a radiation pattern characterized by many grating lobes that contaminate the value of the brightness temperature associated with the boresight position. In this article, an antenna pattern correction (APC) is proposed to correct these effects. The algorithm takes advantage of an iterative formulation based on the Jacobi Method, providing a suitable correction that depends on the chosen spatial resolution. The APC algorithm was tested at both K- and Ka-bands with similar performance. Here, only the results from the latter are shown, as its antenna pattern is the most challenging among CIMR.

Index Terms— Antenna pattern correction (APC), conical scan, Copernicus Imaging Microwave Radiometer (CIMR), microwave radiometry, radiometric accuracy.

I. INTRODUCTION

MONITORING the Earth's surface and its atmosphere has become increasingly important for understanding climate change within the framework of global warming. This is particularly important for polar regions, where ice loss and coastal erosion have dramatically increased during the last decades. Indeed, the Arctic surface air temperature has increased by more than double the global average over the last two decades, with feedback from the loss of sea ice and snow cover contributing to amplified warming [1]. Within this framework, microwave radiometry is an important

tool for monitoring the polar regions, as recognized in [2]. In particular, the need for specific Earth observation products, such as the sea ice concentration (SIC) and the sea surface temperature (SST) at a nominal 10-km ground resolution, with at least a daily revisit time, was identified as being crucial [2].

Currently available satellite products at 10-km resolution are obtained by resampling the native radiometric measurements [3]. This is why a new mission called Copernicus Imaging Microwave Radiometer (CIMR) with improved ground resolution capabilities has been identified by the European Community as being one of the six Copernicus high-priority candidate missions (HPCMs) that will be developed in the next ten years [4]. CIMR requirements are stringent: spatial resolution ≤5 km with an uncertainty of ≤5%, with respect to SIC and sea ice extent (SIE), and spatial resolution ≤15 km and an uncertainty ≤0.2 K for SST demand (with highly accurate measurements).

The CIMR instrument is designed as a conically scanning imaging microwave radiometer that acquires continuous and contiguous measurements along the forward and backward scan. As reported in [5], the CIMR antenna foresees a deployable mesh reflector with a diameter of about 7 m, to accommodate the required coverage and spatial resolution within the applicable mass and volume constraints.

The antenna dimensions determine the spatial resolution, which is defined by the instantaneous field of view (IFOV), i.e., the region where the received power is within −3 dB below the maximum. Nevertheless, the measurements collected by the spaceborne radiometer are characterized by undesired contributions: 1) contamination coming from the region outside the IFOV (e.g., cosmic microwave background, lunar and solar contributions, and galaxy emissions); 2) cross-polarization coupling; and 3) energy collected by side and grating lobes. In order to mitigate contributions of types 1) and 2), antenna pattern correction (APC) algorithms were developed [6], [7], [8], [9] and are recalled in [5], to which the reader is referred to for deeper insight. More specifically, a preliminary approach to the correction of these effects is presented in [5], but with simplified assumptions about the acquisition geometry. The mitigation of the grating lobe contamination, singling out the brightness temperature T_b of the scenario within the IFOV, was obtained from the antenna temperature associated with the entire radiation pattern, i.e., over the 4π solid angle, through the implementation of a well-established image processing approach and based on the use of deconvolution techniques [10], [11]. The method

was applied at the image level, assuming that the measured temperature values were recomposed to form a raster from the punctual observations.

As in [5], the proposed APC only considers the most energetic contributions of the antenna pattern, which are defined and limited by a proper threshold value of the normalized antenna gain. The choice of this threshold value is heuristically driven, but it can be adapted to other cases, depending on the antenna characteristics and the error and accuracy constraints on the brightness temperature and/or the EO products. In this present article, the chosen threshold value is -52 dB, with respect to the normalized maximum, so that the contributions to the measurements, besides the main beam, include the sidelobes and the more energetic grating lobes (up to $>99\%$ of the radiated energy) [5].

The APCs are an attempt to obtain the brightness temperature values T_b from the antenna measurements pertaining only to the angular directions that define the spatial area of interest, such as the footprint or a wider area surrounding the boresight direction. Hence, the main disturbances 2) must be properly compensated to obtain an accurate estimate of the main beam brightness temperature.

In this article, an APC method for correcting CIMR measurements, collected in ungridded instrument geometry, is described and tested over synthetic scenarios. In the algorithm, the contributions from 1) and 2) are assumed to have been previously compensated. It is worth noting that this algorithm, although specifically designed for the CIMR mission, can be applied to other conical scanning instruments.

The proposed APC works channel-by-channel, correcting all feed measurements together. It has been tested over K- and Ka-bands, but the presented results only refer to the Ka channel because it has the most challenging antenna pattern, i.e., it exhibits the strongest contamination due to side and grating lobes.

This article is organized as follows. In Section II, the geometry of the acquisition model is introduced, along with the statement of the APC problem and the description of the forward model (i.e., the model used to simulate the measurement process). Section III deals with the description of the theoretical APC, its limits, and the algorithm devised for operative use. The results obtained with the proposed APC are described in Section IV, for several different synthetic scenes intended to stress the algorithm. Finally, the results obtained are discussed in Section V.

II. ACQUISITION MODEL

In this section, the acquisition geometry and the APC algorithm are formalized to provide a comprehensive framework for the understanding of the theoretical and iterative APC (see Section III).

The CIMR instrument will observe the Earth at L-, C-, X-, K-, and Ka-bands from a platform that moves in a polar orbit, at an average altitude of approximately 836 km and with an observation zenith angle of $55.0° \pm 1.5°$, by performing a conical scan at a rotation speed equal to 7.8 r/min [4]. The conical scan and the varying height of the satellite orbit, with respect to the Earth, produce an irregular sampling grid over the Earth's surface. In order to meet the mission requirements [5], L-, C-/X-, and K-/Ka-bands have one, four, and eight feeds, respectively. The sampling period and spatial resolution depend on the specific channel.

A. Instrument Geometry

Given a generic channel of CIMR, let $u = 0, 1, \ldots, U - 1$ be the index spanning the feed number and T_s the sampling time. Let us also set the reference time $t = 0$ and an orbit state vector that uniquely defines the CIMR position along its trajectory. Then, the boresight of the antenna pattern of the uth feed points at the position $r[u, n']$ on the Earth's surface at the sampling instant $t = n' \cdot T_s$, $n' = 0, 1, \ldots, N' - 1$, with N' the number of time instants. After one sampling period T_s, the feed boresight moves on the subsequent point $r[u, n' + 1]$ on the Earth's surface and so on, thus defining a sequence of points. The curve interpolating these points is the scan trajectory of the uth feed, while Fig. 1(a) provides a sketch of the scan geometry of one feed of the Ka channel, Fig. 1(b) shows the coverage of the eight feeds over a limited region on the Earth's surface. The set of the points corresponding to the boresight positions on the Earth's surface of all feeds at all sampling instants defines the CIMR reference grid. The conical scanning produces an irregular reference grid, as shown in Fig. 1(a), where the sampling period is set to 0.72 e^{-4} s [4], which corresponds to an approximate 0.55-km step on a locally flat Earth surface. It can be observed that the along-scan resolution (fine, dictated by the subsampling time) is very different from the across-scan resolution (coarse, dictated by the rotation period, the satellite velocity and the number of feeds and their position in the focal plane). Furthermore, the trajectories and relative position of the sampling points vary strongly, according to the region of the swath that is considered (central or lateral).

In the following, each pair $[u, n']$ is replaced by a unique index $= N'u + n'$, which, by extension, corresponds to the boresight position $r[n] \equiv r[u, n']$. The following relations hold that:

$$n \leftrightarrow [u, n'] \leftrightarrow r[u, n'] \leftrightarrow r[n]. \tag{1}$$

Equation (1) defines a unique indexing rule over the Earth's surface as it is determined by the instrument acquisition geometry for a given orbit state vector. For the sake of convenience, n is referred to as a "point" or "boresight position" or "instant" according to its dual meaning in space and time.

A mesh is usually adopted to perform basic operations over an irregular geometry in a systematic and relatively efficient way, such as point location and interpolation. In this work, a Delaunay triangulation of the CIMR reference grid points is used [12]. The Delaunay triangulation is widely used in several engineering fields, such as well-known FEM software distributions (CST Studio Suite, Ansys HFSS, and Altair Feko), because of its favorable geometrical properties and quick computation. In Fig. 2, two examples of Delaunay triangulation built upon the CIMR reference grid in the Ka-band are reported for a central and a peripheral region of the swath.

B. APC Problem Statement

The top-of-atmosphere (TOA) brightness temperature, measured by CIMR at point n (also known as antenna temperature), is indicated by $T_A[n]$ and can generally be expressed as

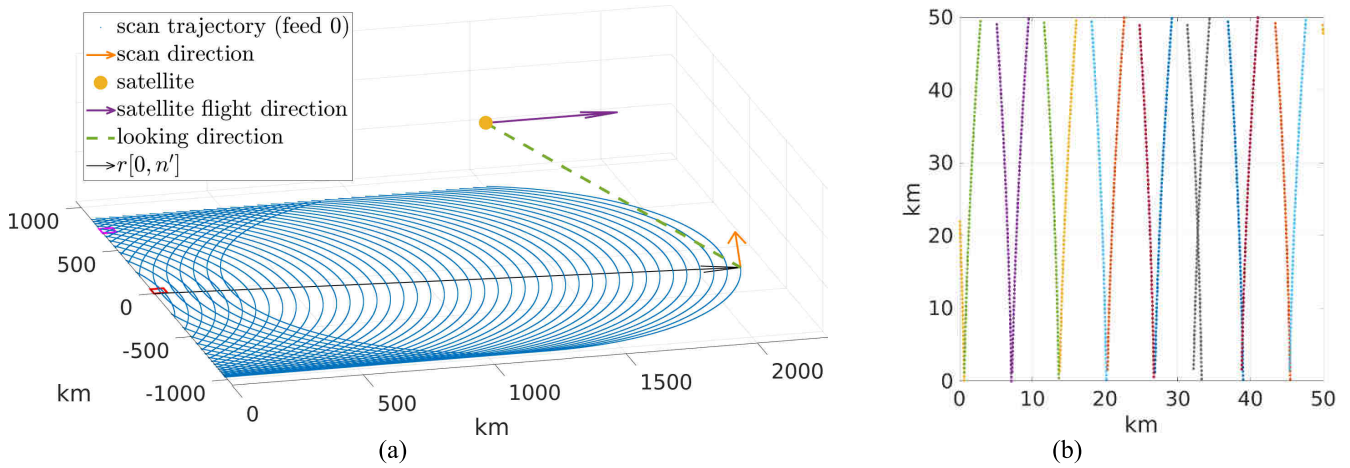$$T_A[n] = \int A_n(r)T_b(r)dr + \delta[n] \tag{2}$$

Fig. 1.   Instrument geometry. (a) Scan trajectory of one feed of the CIMR system in Ka-band. (b) Zoom of the red square of (a), reporting the trajectories and the subsampling points of eight feeds (one color = one feed).
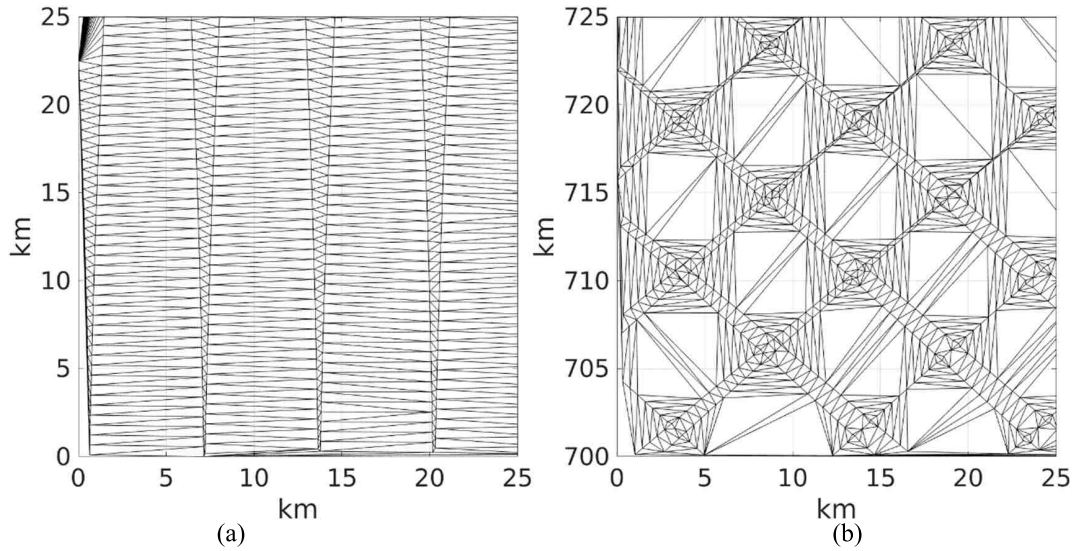

Fig. 2.   Delaunay mesh built upon the CIMR reference grid inside the red square of Fig. 1(a). (b) Delaunay mesh built upon the CIMR reference grid inside the magenta square of Fig. 1(a). The solid lines in (a) and (b) are the edges of the Delaunay triangles whose vertices are the boresight positions projected onto the Earth's surface.

where A_n is the projection of the antenna pattern on the Earth's surface when the boresight points to $\boldsymbol{r}[n]$, T_b is the space-continuous TOA brightness temperature of the scene, and $\delta[n]$ accounts for second-order contributions, such as back lobes, cross-polarization effects, measurement noise, and nonlinear effects. The antenna pattern projection A_n changes as the satellite and the Earth reciprocally move; furthermore, the passive system condition of the antenna pattern holds

$$\int A_n \leq 1 \quad \forall n. \tag{3}$$

Equation (2) states that $\boldsymbol{T}_A$ may consistently deviate from T_b because of the contamination coming from areas outside the angular region of interest (i.e., IFOV or main beam). The effect of antenna pattern smearing on each $\boldsymbol{T}_A[n]$ is not evaluated in this study.

With the purpose of evaluating the performances of the proposed APC, where the real antenna pattern is used, an ideal system is introduced. For the latter, the actual antenna pattern is replaced by an ideal one, which assumes a constant value inside a given aperture angle and is zero elsewhere. The possible aperture angles are either $\theta_{-3\text{dB}}$ or $2.5\theta_{-3\text{dB}}$, which correspond to the IFOV and the main beam, respectively [4]. In the following, the numerical domain that corresponds to the ground projection of the ideal antenna pattern is indicated by the term SUPPORT. In accordance with (2), the TOA brightness temperature collected by the ideal system at position n is

$$\boldsymbol{T}_{A_{\text{ideal}}}[n] = \int A_n^{\text{ideal}}(\boldsymbol{r}) T_b(\boldsymbol{r}) d\boldsymbol{r} \tag{4}$$

where A_n^{ideal} is the projection of the ideal antenna pattern when the boresight points to $\boldsymbol{r}[n]$. The acquisition error of the CIMR system is defined as the difference between the synthetic measurement and the ideal one

$$\boldsymbol{e} = \boldsymbol{T}_A - \boldsymbol{T}_{A_{\text{ideal}}}. \tag{5}$$
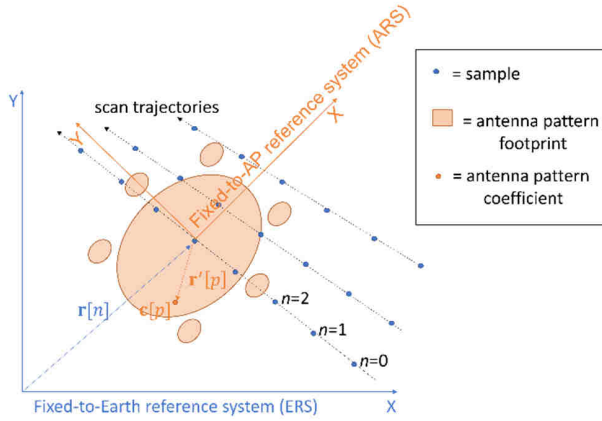
Fig. 3. Reference systems used to define the forward model. The large ellipsis is the sketch of the footprint encompassing the main beam and secondary lobes; the smallest ones represent the footprint of the grating lobes.

The APC algorithm is applied to limit the acquisition error of the CIMR system. Specifically, the goal of the APC is to produce an estimate of the ideal value at sample n by potentially using all the available observations $\boldsymbol{T}_A$

$$\hat{\boldsymbol{T}}_{A\,\text{ideal}} = \text{APC}(\boldsymbol{T}_A). \tag{6}$$

The APC produces an APC error

$$\boldsymbol{e}_{\text{APC}} = \hat{\boldsymbol{T}}_{A\,\text{ideal}} - \boldsymbol{T}_{A_{\text{ideal}}}. \tag{7}$$

C. Forward Model for Instrument Geometry

In order to calculate $\boldsymbol{T}_A[n]$, the integral equation in (2) is approximated by discretizing the antenna pattern. Let $p = 0, 1, \ldots, P - 1$ be the index over the antenna pattern grid, fixed with respect to the antenna pattern reference system to which are associated a position $\boldsymbol{r}'[p]$ and an antenna pattern coefficient $\boldsymbol{c}[p]$. These geometrical parameters are shown in Fig. 3. The following three assumptions are made:

$$\boldsymbol{c}[p] \geq 0 \quad \forall p \in [0, P - 1] \tag{8a}$$

$$\sum_{p=0}^{P-1} \boldsymbol{c}[p] = C \leq 1 \tag{8b}$$

$$p = 0 \text{ corresponds to the boresight position.} \tag{8c}$$

The assumptions in (8a) and (8b) are consistent with a passive system, whereas (8c) sets the convention on the indexing order of the antenna pattern coefficients.

In the following, the second-order impairments are either considered as being compensated before the APC module or their contribution is assumed to be negligible with respect to the contamination introduced by secondary and grating lobes. Hence, the term $\delta[n]$ is dropped and (2) is approximated as

$$\boldsymbol{T}_A[n] = \sum_{p=0}^{P-1} \boldsymbol{c}[p] T_b(f(n, p)) \tag{9}$$

where $f(n, p)$ is a function that maps $\boldsymbol{r}'[p]$ to the corresponding point in the fixed-to-Earth reference system when the boresight points to $\boldsymbol{r}[n]$.
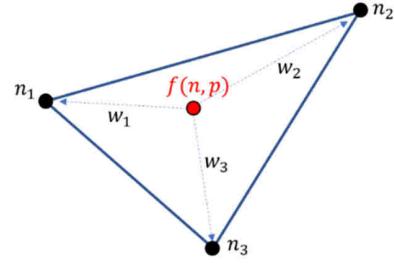

Fig. 4. Interpolation by means of barycentric coordinates of a triangle defined over three grid points. w_1, w_2, and w_3 are the barycentric coordinates of the query point $f(n, p)$ with respect to n_1, n_2, and n_3.

It should be noted that $T_b(f(n, 0)) = T_b(\boldsymbol{r}[n])$, by construction, i.e., the boresight always points to a node on the CIMR grid. Equation (9) is not useful for the APC in this form because T_b is continuous, whereas $\boldsymbol{T}_A$ is sampled over the CIMR reference grid. Hence, T_b is sampled to obtain the column vector of TOA brightness temperature samples over the CIMR reference grid, namely, $\boldsymbol{T}_b$, as

$$\boldsymbol{T}_b[n] = T_b(\boldsymbol{r}[n]) \quad \forall \tag{10}$$

For each pair (n, p), one of the following two cases occurs. If $f(n, p)$ is inside the mesh, $T_b(f(n, p))$ is approximated by means of interpolation over the mesh; otherwise, $T_b(f(n, p))$ is cast to a boundary condition. The former is the most frequent scenario, which occurs for all positions p for which the boresight position is sufficiently far from the mesh border, and its value is a function of the value in the vertices of the enclosing triangle, weighted by their barycentric coordinates (see Fig. 4).

The previous assumptions lead us to rewrite (9) as the system forward model, defined over the instrument geometry (see Appendix A for the mathematical derivation)

$$\boldsymbol{T}_A = \mathbf{A}\boldsymbol{T}_b + \mathbf{D}\boldsymbol{c} \tag{11}$$

where $\boldsymbol{A}$ is the $N \times N$ system matrix projecting the TOA brightness temperature onto the CIMR grid. It has the properties described in the following (the proofs are provided in Appendix A).

1) All entries are nonnegative

$$A[n, m] \geq 0 \quad \forall n, \ m. \tag{12}$$

2) The coefficient $A[n, n]$, associated with the boresight position, is lower bounded by the antenna pattern coefficient in the boresight position

$$A[n, n] \geq \boldsymbol{c}[0] \quad \forall \tag{13}$$

3) The sum of each row is upper bounded by the overall gain of the (discretized) antenna pattern

$$\sum_{m=0}^{N-1} \mathbf{A}[n, m] \leq \sum_{p=0}^{P-1} \boldsymbol{c}[p] \quad \forall n \tag{14}$$

where the equality holds if, and only if, all the nonzero antenna pattern coefficients are inside the mesh.

4) It is linear with respect to the antenna pattern coefficients

$$\boldsymbol{c} = \boldsymbol{c_1} + \boldsymbol{c_2} \Rightarrow A = A_1 + A_2 \tag{15}$$

where A_1 and A_2 are matrices associated with $\boldsymbol{c_1}$ and $\boldsymbol{c_2}$, respectively.

5) Each row is, at most, $(3P - 2)$-sparse. The actual sparsity for a common antenna pattern is even lower because the nonzero antenna pattern coefficients cluster in the antenna pattern beams. As $P \ll N$, most of the entries are zero. Therefore, A can be efficiently stored by using a sparse matrix representation.

$\mathbf{D}$ is the $N \times P$ boundary condition matrix so that vector $\mathbf{D}c$ accounts for the boundary conditions, i.e., the contribution of the TOA brightness temperature outside the mesh on the measurements T_A. It is a structured matrix; the rows of $\mathbf{D}$ corresponding to boresight positions (which are sufficiently far from the mesh border) are identically equal to zero.

D. Forward Model of Ideal Antenna Pattern

The forward model of the ideal antenna pattern is the forward model associated with the ideal system. The ideal antenna pattern coefficients $c_{\text{ideal}}[p]$, $p = 0, 1, \ldots, P - 1$ are defined over the antenna pattern sampling grid and satisfy the conditions in (8a)–(8c). Without loss of generality, it is assumed that the numbering of the sampling grid positions $r'[p]$ is such that the first P_{SUPPORT} antenna pattern coefficients are inside the support. For instance, if the ideal antenna pattern is uniform, then

$$c_{\text{ideal}}[p] = \begin{cases} \dfrac{1}{P_{\text{SUPPORT}}}, & \text{if } 0 \le p < P_{\text{SUPPORT}} \\ 0, & \text{otherwise.} \end{cases} \qquad (16)$$

Thus, the forward model of the ideal antenna pattern can generally be written as

$$T_{A_{\text{ideal}}} = A_{\text{ideal}} T_b + d_{\text{ideal}} \qquad (17)$$

where $T_{A_{\text{ideal}}}$ is the vector of values produced by the ideal system and A_{ideal} maps the TOA brightness temperature onto the ideal observations. The vector d_{ideal} accounts for the boundary conditions and it is only nonzero near the borders. As for the system forward model, (17) is not intended to be used for simulating the acquisition process.

III. THEORETICAL APC AND PROPOSED APC

In this section, the theoretical APC (the algorithm that provides a zero-error correction) is derived from matrix algebra argumentations and discussed. In the second part, the proposed operative APC (called "APC-i," where "I" stands for iterative) is presented.

A. Theoretical APC and Practical Issues

According to the definition in (7), the "zero-error APC" must provide $e_{\text{APC}} = \mathbf{0}$. Let $\text{null}(\mathbf{B})$ and $\mathbf{B}^{\dagger}$ be an orthonormal base, spanning the null space, and the Moore–Penrose pseudoinverse of a square matrix $\mathbf{B}$, respectively. If $\text{null}(A) \subseteq \text{null}(A_{\text{ideal}})$, the expression of the zero-error APC is (Appendix B)

$$\hat{T}_{A_{\text{ideal}}}^{\text{opt}} = A_{\text{ideal}} A^{\dagger}(T_A - \mathbf{D}c) + d_{\text{ideal}}. \qquad (18)$$

If $\text{null}(A) \nsubseteq \text{null}(A_{\text{ideal}})$, then no zero-error APCs[1] exist. Indeed, it can be shown that there are infinitely many T_b mapped onto the same T_A but different $T_{A_{\text{ideal}}}$, leading to ambiguities in the correction process. In such a case, it is

necessary to set up additional constraints and pick up a metric to minimize, e.g., $\|e_{\text{APC}}\|_2$, to derive the expression of the theoretical APC in that sense. Nevertheless, this is out of the scope of this study.

In a realistic scenario, A is nonsingular and $A^{\dagger} \equiv A^{-1}$. Nevertheless, A is ill-conditioned, due to the relatively low directivity of the antenna pattern with respect to the CIMR reference grid. Details on this aspect are investigated in Appendix C.

The calculation of the Moore–Penrose pseudoinverse or the calculation of the inverse is not necessary because direct or iterative linear system solvers might be used to calculate the vector $A^{-1}(T_A - \mathbf{D}c)$. Direct solvers based on matrix decompositions (e.g., LU decomposition and QR factorization) face the same problems that arise for the inversion. Iterative solvers are tailored for memory-intensive problems, but their convergence is tied to good conditioning of the system matrix. For ill-conditioned matrices, time-based stopping criteria ensure that a solution is provided within a controlled time interval, but these generally provide poor accuracy. On the contrary, constraining the residual error may lead to an unacceptable computational delay in an operational ground segment processing chain. Effective preconditioning matrices can also be provided to ensure a faster convergence of iterative methods, but their computation is often as resource demanding as inverting the original matrix.

Using valid boundary conditions is another key point for the theoretical APC. In the practical usage of (18), the boundary condition matrices $\mathbf{D}$ and d_{ideal} are not precisely known because they represent the TOA brightness temperature outside of the measurement region; they can only be approximated by an a priori model or estimated, e.g., by using the information extracted from previous measurements. If $\hat{\mathbf{D}}$ and $\hat{d}_{\text{ideal}}$, namely the estimated values of $\mathbf{D}$ and d_{ideal}, are used in (18), then the APC error becomes

$$e_{\text{APC}} = A_{\text{ideal}} A^{-1}(\hat{\mathbf{D}} - \mathbf{D})c + (\hat{d}_{\text{ideal}} - d_{\text{ideal}}) \qquad (19)$$

i.e., the zero-error condition is not generally achieved. A general upper boundary on this error also depends on the antenna patterns and its mathematical formulation is beyond the scope of this work. To provide the reader with a numeric example, we consider a 500×1500 km scene that is homogeneously composed by open ocean surrounded by open ocean ($T_b = 130$ K). To estimate the error on boundary conditions, the theoretical APC is applied by wrongly assuming that the scene is surrounded by ice (250 K) instead of open ocean, i.e., the estimation errors $\|\hat{\mathbf{D}} - \mathbf{D}\|$ and $\|\hat{d}_{\text{ideal}} - d_{\text{ideal}}\|$ are maximized. If the antenna pattern reported in Fig. 5 is used, the APC error is of the order of 100 K in the first 2–3 km from the scene boundary but decreases to about 10 K within 10 km and 0.1 K at about 85 km. Beyond 85 km, the error continues to decrease and becomes negligible. Obviously, better information on boundary conditions, which is generally required for satellite product development, leads to better performances.

B. Iterative APC—"APC-i"

The proposed APC method follows a two-phase approach. First, $\widehat{T_b}$, the estimation of t_b, is carried out by means of an iterative algorithm. Then, $\hat{T}_{A_{\text{ideal}}}$ is computed by applying the ideal forward model to $\widehat{T_b}$.
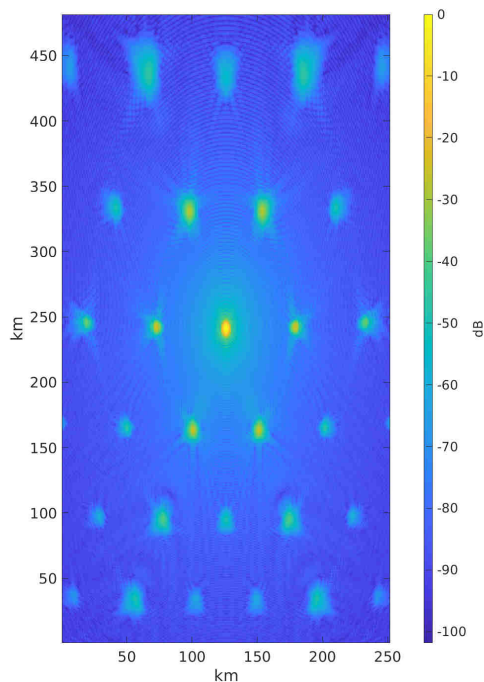
---

[1] Zero-error Bayesian APC might exist for $\text{null}(A) \nsubseteq \text{null}(A_{\text{ideal}})$. However, we are only considering the class of deterministic algorithms.

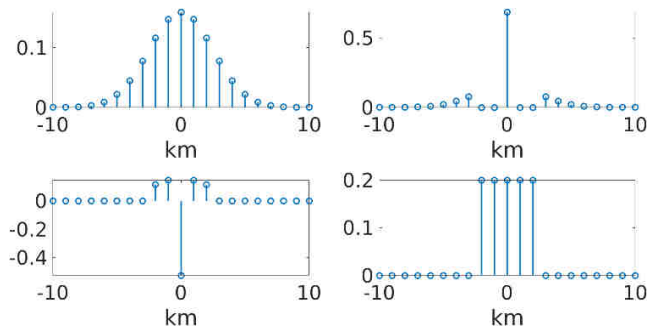Fig. 5. Ka-band antenna pattern used for assessing the APC performances.

Fig. 6. Comparison among the considered antenna patterns, simplified in 1-D sketches. Assuming the FOCUS region extended over five samples, the figure shows (Left to Right and Top to Bottom) the antenna pattern, the concentrated antenna pattern, the mismatch, and the uniform ideal antenna pattern (SUPPORT is assumed coincident to the FOCUS).

Let us define FOCUS as being the spatial region centered on the boresight, with c_{FOCUS} being the overall gain of the antenna pattern inside it. We assume that the latter is greater than $C/2$, i.e.,

$$c_{\text{FOCUS}} = \sum_{p=0}^{P_{\text{FOCUS}}-1} \boldsymbol{c}[p] > \frac{C}{2} \tag{20}$$

where it is supposed that, without loss of generality, the first P_{FOCUS} coefficients of the antenna pattern belong to FOCUS.

1) Proposed Algorithm: Let us define the concentrated antenna pattern coefficients $\boldsymbol{c}'$ as

$$\boldsymbol{c}'[p] = \begin{cases} c_{\text{FOCUS}}, & \text{if } p = 0 \\ 0, & \text{if } 0 < p < P_{\text{FOCUS}} \\ \boldsymbol{c}[p], & \text{otherwise} \end{cases} \tag{21}$$

and the mismatch $\boldsymbol{\Delta}_c$ as

$$\boldsymbol{\Delta}_c = \begin{cases} -c_{\text{FOCUS}} + \boldsymbol{c}[0], & \text{if } p = 0 \\ \boldsymbol{c}[p], & \text{if } 0 < p < P_{\text{FOCUS}} \\ 0, & \text{otherwise} \end{cases} \tag{22}$$

such that

$$\boldsymbol{c}' = \mathbf{c} - \boldsymbol{\Delta}_c. \tag{23}$$

The concentrated antenna pattern is a hypothetical antenna pattern whose gain inside the FOCUS region is c_{FOCUS} and it is fully concentrated in the boresight position. On the contrary, the concentrated antenna pattern corresponds to the real antenna pattern outside the FOCUS region. The mismatch $\boldsymbol{\Delta}_c$ is a nonphysical quantity given by the difference between the actual and the concentrated antenna patterns; its support is limited to the FOCUS region, where it is equal to the actual antenna pattern except in the boresight position, where

its value is nonpositive. The sketches in Fig. 6 report an illustrative comparison of the aforementioned antenna patterns.

The system matrix can be split by using the property in (15), yielding

$$A' = \mathbf{A} - \boldsymbol{\Delta}_A. \tag{24}$$

As $\boldsymbol{c}'$ fulfills (8a)–(8c), A' is the system matrix of the concentrated antenna pattern that depends on the chosen FOCUS; it satisfies all the properties listed in Section II-C. On the contrary, $\boldsymbol{\Delta}_A$ is not a valid system matrix.

Given a suitable number of iterations, $l > 1$, and the estimation of the boundary conditions $\hat{\mathbf{D}}$ and $\hat{\boldsymbol{d}}_{\text{ideal}}$, the proposed APC algorithm is structured as follows:

1) Solve $\boldsymbol{T}_A = A'\boldsymbol{T}_b + \hat{\mathbf{D}}\boldsymbol{c}$ by means of the Jacobi method

$$\begin{aligned} \widehat{\boldsymbol{T}_b}^{(l)} = \text{diag}(A')^{-1} \big\{ & (\boldsymbol{T}_A - \hat{\mathbf{D}}\boldsymbol{c}) \\ & - [A' - \text{diag}(A')]\widehat{\boldsymbol{T}_b}^{(l-1)} \big\} \end{aligned} \tag{25}$$

where $\text{diag}(A')$ is the diagonal matrix made by the main diagonal of A' and $\widehat{\boldsymbol{T}_b}^{(0)} = \boldsymbol{T}_A - \hat{\mathbf{D}}\boldsymbol{c}$. Equation (25) is the vector form of the Jacobi method.

2) Compute $\widehat{\boldsymbol{T}}_{A\text{ideal}}$ through (17), where $\boldsymbol{T}_b$ is replaced with $\widehat{\boldsymbol{T}_b}^{(l)}$ and $\boldsymbol{d}_{\text{ideal}}$ with $\hat{\boldsymbol{d}}_{\text{ideal}}$

$$\widehat{\boldsymbol{T}}_{A\text{ideal}} = A_{\text{ideal}}\widehat{\boldsymbol{T}_b}^{(l)} + \hat{\boldsymbol{d}}_{\text{ideal}}. \tag{26}$$

2) Convergence: A necessary and sufficient condition for (25) to converge [13] is

$$\rho\left(\mathbf{I} - \text{diag}(A')^{-1}A'\right) < 1 \tag{27}$$

where $\rho(\cdot)$ is the spectral radius. The previous condition holds if A' is strictly diagonally dominant (sufficient condition), i.e.,

$$\big|A'[n,n]\big| - \sum_{m,m \neq n} \big|A'[n,m]\big| > 0 \quad \forall n \tag{28}$$

and implies (27). The concentrated system matrix is strictly diagonally dominant by construction; hence, the Jacobi method converges. The proof is provided in Appendix D. The Jacobi method has been chosen among other iterative solvers [e.g., generalized minimal residual method (GMRES)], for its plain and memory-efficient implementation. Moreover, the form of the Jacobi method provides some insights for interpreting the proposed algorithm.

3) Interpretation: The first step of the proposed algorithm estimates the TOA brightness temperature over the CIMR reference grid, as if the concentrated antenna pattern was used in the sensing process. For such an antenna pattern, the generally discrete forward model is given by (9) and (21), for comparison

$$T_A[n] = c_{\text{FOCUS}} T_b(r[n]) + \sum_{p=P_{\text{FOCUS}}}^{P-1} c'[p] T_b(f(n, p)). \quad (29)$$

Equation (25) is rewritten, after manipulation, as

$$\widehat{T_b}^{(l)}[n] = \frac{1}{c_{\text{FOCUS}}} \left[T_A[n] - \sum_{p=P_{\text{FOCUS}}}^{P-1} c'[p] \widetilde{T}_b^{(l-1)}(f(n, p)) \right] \quad (30)$$

where $\widetilde{T}_b^{(l-1)}(f(n, p))$ indicates either the interpolation of $\widehat{T_b}^{(l)}$ in $f(n, p)$, when $f(n, p)$ is inside the mesh, or the estimated boundary condition, otherwise. It is the scalar form of the Jacobi method and also corresponds to (29) by multiplying by c_{FOCUS} and replacing $\widetilde{T}_b^{(l-1)}(f(n, p))$ and $\widehat{T_b}^{(l)}[n]$ by $T_b(f(n, p))$ and $T_b(r[n])$, respectively. Each step of the proposed method can be interpreted as the inversion of the generally discrete forward model of the concentrated antenna pattern, where the (unknown) TOA brightness temperature outside the boresight position is replaced by the last available estimation. Iterating over (30) is guaranteed to converge since A' is strictly diagonally dominant. The same reasoning can be repeated using the system forward matrix A instead of A' inside the Jacobi method; then, (30) becomes

$$\widehat{T_b}^{(l)}[n] = \frac{1}{c_0} \left[T_A[n] - \sum_{p=0}^{P-1} c[p] \widetilde{T}_b^{(l-1)}(f(n, p)) \right]. \quad (31)$$

The last relation may suggest that it can be iterated over, i.e., applying the Jacobi method on the system matrix to exactly solve the APC problem. Nevertheless, this procedure does not converge because the system matrix A, associated with CIMR simulations, fails to satisfy (27).

4) Error Analysis: The error of the proposed APC algorithm at iteration l is

$$\begin{aligned} e_{\text{APC}} &= \widehat{T_{A_{\text{ideal}}}} - T_{A_{\text{ideal}}} \\ &= A_{\text{ideal}} \widehat{T_b} + \hat{d}_{\text{ideal}} - A_{\text{ideal}} T_b - d_{\text{ideal}} \quad (32) \end{aligned}$$

where (26) and (17) have been substituted in (7).

Let us assume l to be sufficiently large such that $\widehat{T_b}^{(l)}$ converges to $A'^{-1}(T_A - \hat{D}c)$; substituting in the previous relation yields

$$\begin{aligned} e_{\text{APC}} &= A_{\text{ideal}} A'^{-1}(T_A - \hat{D}c) \\ &\quad - A_{\text{ideal}} T_b + \hat{d}_{\text{ideal}} - d_{\text{ideal}}. \quad (33) \end{aligned}$$

By substituting in (11) and (24) and considering that $A'^{-1}A' = I$, the previous relation becomes

$$\begin{aligned} e_{\text{APC}} &= A_{\text{ideal}} A'^{-1} \Delta_A T_b \\ &\quad + \left[A_{\text{ideal}} A'^{-1}(D - \hat{D}) \right] c + \hat{d}_{\text{ideal}} - d_{\text{ideal}}. \quad (34) \end{aligned}$$

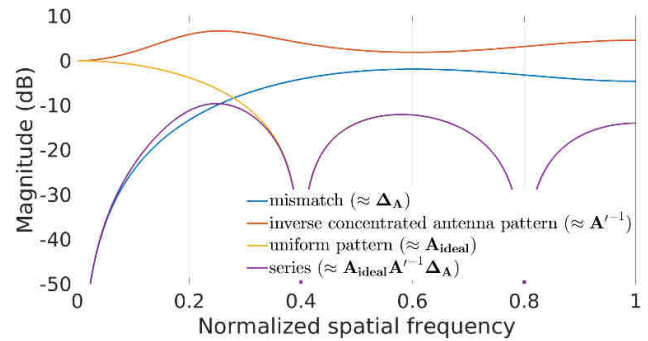The APC error is the sum of two terms: the mismatch error (first row of the second member) and the boundary conditions

Fig. 7. Frequency response of the digital filters "similar" to the effects of the matrices A_{ideal}, A'^{-1} and Δ_A.

error (last row). The mismatch error arises from using the concentrated antenna pattern instead of the original one to estimate the TOA brightness temperature. The expression $A_{\text{ideal}} A'^{-1} \Delta_A T_b$ can be qualitatively evaluated by comparing the effects of such matrices to those of "similar" digital linear filters.[2] A comparison of the frequency response of such filters is proposed in Fig. 7 by using the impulse responses shown in Fig. 6. A_{ideal} behaves as a low-pass filter because it is associated with a uniform and spatially limited antenna pattern. A'^{-1} can be considered as a hybrid between an all-pass filter and a band/high-pass filter since it corresponds to the inversion of the concentrated system matrix. Δ_A has high-pass behavior since the mismatch Δ_c sums to 0. As a consequence of the latter, the mismatch error tends to 0 over uniform t_b.

The boundary condition error has already been discussed for the theoretical APC. From Fig. 7, the term $A_{\text{ideal}} A'^{-1}$ can be framed as a low-pass filter. As will be shown by the simulation results, a good coarse estimation of the boundary condition matrix D is sufficient to limit the spread of the boundary condition error.

5) Choice of the FOCUS Region: The convergence of the proposed method depends on the choice of the FOCUS region. The convergence rate increases with increasing FOCUS extension, with the drawback of a greater mismatch error due to the increased norm of Δ_A. As the latter has high-pass behavior, the error is expected to impact more severely in the areas where the TOA brightness temperature exhibits spatial variations, i.e., steep transition regions. Changing the FOCUS extension and the associated gain coefficient is also valid in the other sense. If c_{FOCUS} is greater than $C/2$, a narrow region can be chosen to achieve a lower mismatch error, accepting a slower convergence rate. It should be noted that finite precision arithmetic might become critical for convergence when the gain in the FOCUS region gets too close to $C/2$.

Interestingly, the convergence does not depend on how the gain spreads outside the FOCUS, i.e., if there are secondary or grating lobes, nor on how far away they are from the main beam. On the other side, the gain spread is correlated with the number of the boundary condition terms: the farthest the grating lobes, the higher the number of rows in D that are nonzero, i.e., more measurements are directly influenced by the boundary conditions.

---

[2]It is remarked that such matrices represent space-variant linear operators and, therefore, cannot mathematically correspond to digital linear filters.
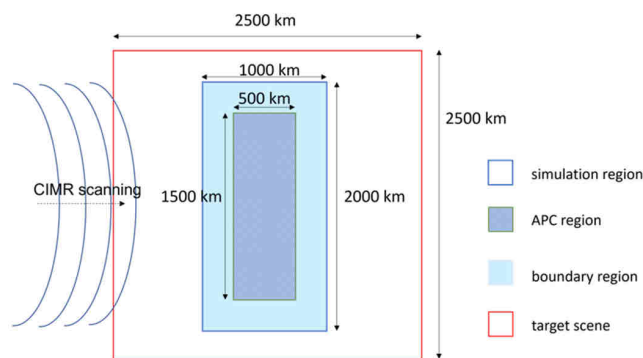
Fig. 8. Geometry of the testbed.

IV. EXPERIMENTAL RESULTS

A. Simulation Setup

The simulation setup was arranged to reproduce the scanning process of CIMR in a simplified manner, according to the following assumptions.

1) The acquisition kinematics are simulated in a 2-D ground-projected geometry.
2) The satellite moves at uniform velocity (6670 m/s) with respect to the Earth's surface, which is considered to be locally flat.
3) The system has eight feedhorns, as for the Ka-bands of CIMR. The positions of feed footprints are fixed and arbitrarily set to obtain an approximately uniform surface coverage.
4) All feeds are assumed to have the same, but offset, pattern. The antenna pattern used is represented in Fig. 5. It was preprocessed by resampling it at a 1-km ground resolution and clipping it below -52 dB. The discretization in pixels of 1×1 km introduces an error of an order of magnitude of about one-hundredth of K in the antenna pattern, thus enabling fast computation while fulfilling the required precision [5].
5) Only translation and rotation of the antenna pattern are considered according to the scanning process, i.e., no antenna pattern distortion due to the variable projection of the swath over the Earth's surface is simulated.

The conical scan period and the sampling time are 7.6923 s and 7.2 e^{-4} s, respectively, according to [4].

B. Testbed

All of the scenarios were simulated according to the geometry shown in Fig. 8. The satellite was assumed to move horizontally from left to right over the target scene and the conical scan rotated counterclockwise. The target scene extension was fixed to 2501 × 2501 km and had a resolution of 1 km.

The forward models were applied to the simulation region placed in the middle of the target scene to generate the measurements. The APC was applied to an inner portion of the simulation region, namely the APC region. The extension of the APC region was chosen such that the grating lobes never exceeded the border of the simulation region. The outer part of the simulation region was the boundary region, chosen such that the grating lobes never exceeded the border of the target scene.
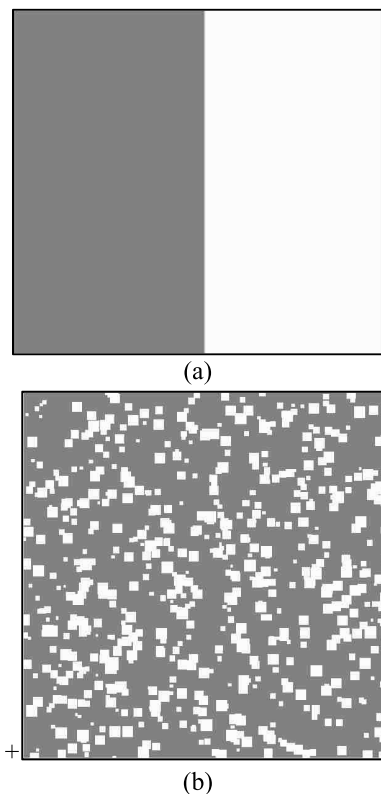

Fig. 9. Two binary target scenes: (a) infinite transition and (b) random ice. White and gray colors correspond to 250 and 130 K TOA brightness temperatures, respectively.

The simulation region was covered by approximately 1.48×10^6 samples; the number of samples inside the solving region was $N \approx 4.72 \times 10^5$; the nonzero antenna pattern coefficients were $P = 1750$. The system matrix $\boldsymbol{A}$ and the concentrated system matrix $\boldsymbol{A}'$ have approximately 5.5×10^8 nonzero entries.

The boundary conditions in the APC are set by assuming that the TOA brightness temperature in the boundary region corresponds to the measurements. This choice provides a coarse estimation of the conditions at the borders, but it is reasonable if no other information is available. Moreover, this guarantees that the compared APCs are fully and equally unaware of the underlying ground truth.

C. Performance Assessment

Two binary target scenes, whose values (130 and 250 K) were chosen according to the CIMR requirements [4], were considered:

1) infinite transition, shown in Fig. 9(a);
2) random ice, shown in Fig. 9(b): random pattern of squares whose sides are randomly generated according to a uniform distribution between 20 and 80 km.

The *Picaso* test card, suggested as a benchmark in [4], was also considered when testing the APC algorithms, which is shown in Fig. 10.

The performance assessment was carried out by considering statistics over the APC error. A key metric for the mission is the success rate, which is defined as

$$\frac{100}{N} \sum_{n=0}^{N-1} \begin{cases} 1, & \text{if } |e_{\text{APC}}[n]| < 0.5 \text{ K} \\ 0, & \text{otherwise} \end{cases} \qquad (35)$$

TABLE I
Success Rate in the Tested Scenarios Using the Uniform IFOV as Ideal Antenna Pattern

| Scene	APC	Distance from closest transition (km)								
		0-4	4-5	5-6	6-7	7-8	8-10	10-20	20-50	> 50
infinite transition	# points	8345	1932	1908	1853	1984	3640	19059	56347	371676
	T_A	1.2	0.0	0.0	0.0	0.0	0.0	0.0	4.9	92.1
	theoretical	6.7	15.6	23.7	42.4	54.2	68.7	97.3	99.5	99.1
	APC-i, $l = 1$	5.6	2.5	0.9	0.2	0.0	0.0	0.0	8.1	95.8
	APC-i, $l = 10$	6.5	24.6	41.6	66.1	85.9	99.9	100.0	100.0	100.0
random ice	# points	60909	13058	12892	12424	12030	23338	100594	159258	72241
	T_A	3.3	13.5	16.4	17.7	19.5	20.5	22.3	39.8	86.3
	theoretical	6.3	18.2	26.8	37.8	50.9	66	90.1	98.9	99.8
	APC-i, $l = 1$	0.1	0.0	0.0	0.1	0.2	0.3	0.9	1.2	8.9
	APC-i, $l = 10$	11.8	52.8	69.0	80.8	92.8	100.0	100.0	100.0	100.0
Picaso	# points	227929	49535	49663	49163	48952	98579	489074	1213197	2441348
	T_A	8.8	16.4	18.0	18.3	19.0	19.7	21.0	33.1	94.3
	theoretical	18.0	38.4	50.1	61.4	74.6	87.8	97.0	95.9	96.0
	APC-i, $l = 1$	0.3	0.5	0.9	1.5	2.3	3.0	3.4	3.7	61.0
	APC-i, $l = 10$	18.5	58.6	75.0	87.2	96.1	100.0	100.0	100.0	100.0
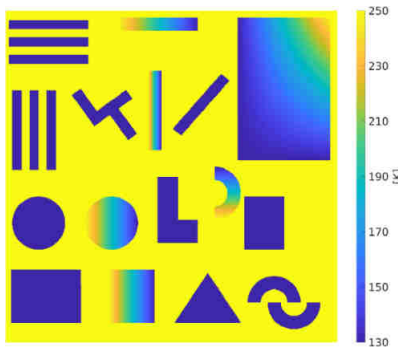
Fig. 10.   Picaso test card.

and this refers to the percentage of points where the absolute APC error is less than 0.5 K. The threshold was chosen according to OBS-1040 in [4] and the samples were grouped according to their distance from the closest transition; the success rate is separately computed for each group. In binary images, the transitions correspond to the brightness discontinuities; in the *Picaso* test card, the transitions are the borders of the geometrical shapes shown in Fig. 10.

D. Results

The uniform IFOV is considered to be an ideal antenna pattern. The performance comparison is carried over two different APC strategies: APC by means of (18), where $\hat{\mathbf{D}}$ and $\hat{\boldsymbol{d}}_{\text{ideal}}$ are used instead of $\mathbf{D}$ and $\boldsymbol{d}_{\text{ideal}}$ ("theoretical"), and APC by means of the proposed method, i.e., (25) followed by (26), ("APC-i").

Metrics related to measurements without APC ("T_A") are also reported for comparison. For APC-I, the FOCUS is set coincident with the SUPPORT. The proposed algorithm is guaranteed to converge because $c_{\text{FOCUS}} \approx 0.58$ for the considered antenna pattern. The related concentrated system

matrix is well-conditioned because the rows are poorly correlated.

In terms of success rate, the results are reported in Table I. For each target scene (first column), the number of samples belonging to each distance-from-closest-transition range is first reported (*# points*); then, the success rates attained by each APC method for each distance range are indicated. For APC-i, the results obtained at one iteration ($l = 1$) and ten iterations ($l = 10$) are also displayed. The red line in the table border identifies the distance corresponding to 1.5 IFOV, which is considered a critical distance to assess the performance of the APC algorithm [4].

Concerning the infinite transition scenario, it clearly emerges that T_A provides very poor results. The results are explained by considering that, when the boresight is within 50 km from the transition line, a large part of the antenna pattern is projected on the opposite side, and it consistently contributes to impair the measurement. The theoretical APC exhibits an improving performance as the distance from the closest transition increases because it attempts to compensate this effect, but it is limited by finite-arithmetic issues. The APC-i performs worse than the theoretical APC, but at the tenth iteration, it attains the best scores in all ranges except the first one. After the tenth iteration, only decimal variation of the success rate is observed; no variation occurs after 23 iterations (not shown here).

Similar results are also obtained in the random ice scenario, as well as in the *Picaso* test card. In order to apply the APC methods to all the geometrical shapes of the latter, ten versions of the target scene are generated by circularly shifting the image in order to cover the entire target scene without increasing the simulation and the solving regions. The APC algorithms are independently applied to each version and the results are finally aggregated. This explains why the number of samples in Table I is about one order of magnitude greater than the other scenarios.

TABLE II

STATISTICS OF APC ERROR (K) IN THE PICASO TEST CARD USING THE UNIFORM IFOV AS IDEAL ANTENNA PATTERN

Statistics	APC	Distance from closest transition (km)								
		0-4	4-5	5-6	6-7	7-8	8-10	10-20	20-50	> 50
Sample Mean	T_A	0.13	0.11	0.11	0.10	0.09	0.09	0.05	0.01	-0.03
	theoretical	0.01	0.07	0.03	0.00	0.00	0.01	0.02	0.03	0.03
	APC-i, $l = 1$	-0.09	-0.05	-0.04	-0.03	-0.05	-0.05	-0.04	-0.01	0.02
	APC-i, $l = 10$	0.02	0.01	0.03	0.02	0.00	0.00	0.00	0.00	0.00
Sample Standard deviation	T_A	6.75	1.27	1.22	1.20	1.19	1.19	1.19	0.97	0.23
	theoretical	4.62	1.72	1.18	0.77	0.56	0.37	0.25	0.31	0.28
	APC-i, $l = 1$	5.47	4.40	2.99	1.90	1.21	0.87	0.79	0.64	0.15
	APC-i, $l = 10$	3.97	2.51	1.55	0.81	0.37	0.18	0.07	0.04	0.01
	APC-i, $l = 23$	7.00	1.10	0.76	0.45	0.20	0.07	0.03	0.03	0.01

TABLE III

SUCCESS RATE IN THE TESTED SCENARIOS USING THE UNIFORM MAIN BEAM AS IDEAL ANTENNA PATTERN

Scene	APC	Distance from closest transition (km)								
		0-4	4-5	5-6	6-7	7-8	8-10	10-20	20-50	> 50
infinite transition	T_A	7.8	8.1	0.0	0.0	0.0	0.0	0.0	4.9	92.2
	theoretical	12.3	14.0	26.7	42.5	54.8	69.4	96.0	99.3	98.6
	APC-i, $l = 2$	5.4	0.0	0.2	9.8	32.6	82.1	99.9	100.0	100.0
	APC-i, $l = 2$, NO IFM	4.4	84.2	100.0	100.0	100.0	100.0	100.0	100.0	100.0
random ice	T_A	5.5	17.4	16.4	17.8	19.4	20.5	22.4	40.0	86.4
	theoretical	17.5	35.1	49.8	64.9	78.1	86.1	98.6	100.0	100.0
	APC-i, $l = 2$	6.3	9.3	30.9	48.8	68.9	93.5	100.0	100.0	100.0
	APC-i, $l = 2$, NO IFM	10.4	90.6	100.0	100.0	100.0	100.0	100.0	100.0	100.0
Picaso	T_A	11.5	20.0	17.9	18.3	19.1	19.7	20.9	33.0	94.3
	theoretical	29.0	46.0	61.8	75.5	84.1	90.6	98.7	98.9	99.2
	APC-i, $l = 2$	12.6	12.5	33.8	56.2	77.8	95.3	100.0	100.0	100.0
	APC-i, $l = 2$, NO IFM	15.5	93.1	100.0	100.0	100.0	100.0	100.0	100.0	100.0

It should be noted that, in all three cases, the success rate at the distance of 1.5 IFOV (red line) varied from 40% to 75% (maximum), and to obtain values higher than 90%, we have to move to 7–10 km (depending on the case). At a 10-km distance, APC-i provides 100% success for all the cases.

In order to appreciate the radiometric distortion introduced by the APC algorithms, the sample mean and the sample standard deviation of the APC error on the *Picaso* test card are proposed in Table II. The former provides information about the bias introduced by the APC methods. The theoretical APC and APC-i perform similarly and never exceed 0.1 K, in terms of absolute value. The sample standard deviation indicates the dispersion of the APC error. For the sake of completeness, the standard deviation at iteration 23 of the proposed method is also reported. We observe that the APC-i shows an improving performance (lower dispersion) as the number of iterations grows, except in the first distance range where it is comparable to T_A. The fact that the dispersion of the APC error substantially decreases from iteration 10 to iteration 23 is not in contrast with the fact that the success rate change is negligible and in the same iteration range: the success rate is a discontinuous statistic, whereas the sample standard deviation is continuous. Thus, performing multiple iterations of the proposed algorithm allows better preservation of the radiometric characteristics of the underlying target scene.

Analogous tests were carried out by considering the uniform main beam as being an ideal antenna pattern. Since $c_{\text{FOCUS}} \approx 0.98$, a very fast convergence occurs in this case. The success rate is reported in Table III. T_A exhibits poor values under 50 km, which are comparable to the same scenario, when using the uniform IFOV as an ideal antenna pattern (Table I). The theoretical APC still suffers from finite-arithmetic effects. The penultimate row reports the scores attained by the proposed algorithm at iteration 2; it underperforms the theoretical APC below the 8-km threshold but outperforms it above. The last row reports the results at iteration 2, before applying the second step of the proposed algorithm, i.e., $\hat{T}_{A\text{ideal}} \equiv \widehat{T_b}^{(l)}$, and it is marked as "NO IFM." A performance boost is observed below the 8-km threshold. This result is explained by considering that the first step of the proposed algorithm has a remarkable low-pass effect near the transitions, due to considering a wide FOCUS. Hence, $\widehat{T_b}^{(l)}$ is a smoothed version of the true T_b that is already close to the target value measured by the ideal system ($T_{A\text{ideal}}$).

Different from the uniform IFOV, in this case, the success rate of the APC-i NO IFM is at 100%, starting from 5 to 6 km in all of the tested scenarios.
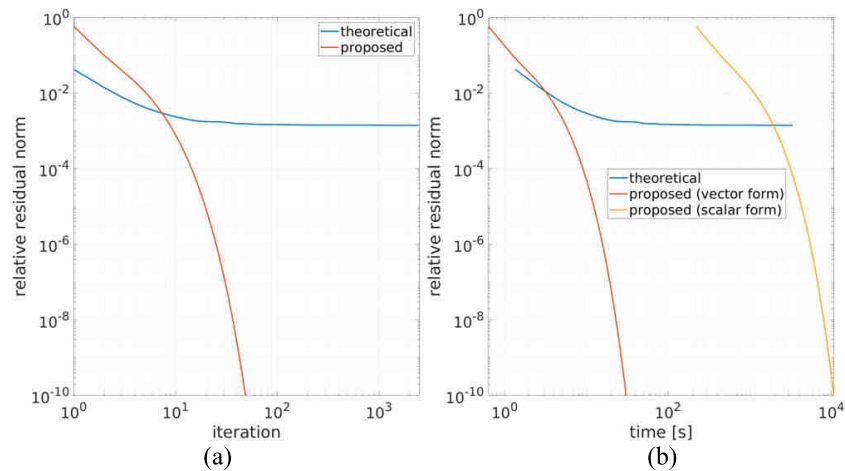
Fig. 11. Computational efficiency of the tested methods on a 500 × 1500 km scene, in terms of (a) algorithm iterations and (b) absolute time.

E. Computational Efficiency

The computational burden of the proposed and the theoretical APCs is mainly determined by the inversion of a linear system.[3] The results presented in this section refer to the processing of a 500 × 1500 km scene.

The efficiency is, therefore, compared in terms of the relative residual norm for an increasing number of iterations. For the proposed algorithm, the relative residual norm at iteration l is (25)

$$\frac{\left\| T_A - \hat{\mathbf{D}}c - \left[\mathrm{diag}(A')^{-1} \left(A' - \mathrm{diag}(A') \right) \hat{T}_b^{(l)} \right] \right\|}{\left\| T_A - \hat{\mathbf{D}}c \right\|}. \quad (36)$$

For the theoretical algorithm, the system $AT_b = (T_A - \mathbf{D}c)$ is iteratively solved by means of the GMRES algorithm and the residual is computed as

$$\frac{\left\| T_A - \hat{\mathbf{D}}c - A\hat{T}_b^{(l_{\mathrm{GMRES}})} \right\|}{\left\| \right.} T_A - \hat{\mathbf{D}}c \quad (37)$$

where l_{GMRES} is the number of iterations of the GMRES algorithm. The iteration versus relative residual norm curves are represented in Fig. 11(a). The curve of theoretical APC is influenced by the ill-conditioning of the system matrix and the convergence is tied to the subspace spanned by the target scene.

On the contrary, the proposed APC does not suffer from ill-conditioning and converges independently of the target scene. According to these results, the relative residual thresholds in the simulations were set to 10^{-3} and 10^{-6} for the theoretical and the proposed APC, respectively. A maximum number of iterations was set to 2500, but only for the former, to face the effects of ill-conditioning.

The plot in Fig. 11(b) compares the relative residual norm, as a function of the absolute computational time. The proposed APC requires less than 30 s to complete 50 iterations (the tail of the red curve) through a MATLAB implementation over an Intel[4] Core[5] i7-8700 CPU @ 3.20 GHz Linux

machine; the theoretical APC takes about 50 min to complete 2500 iterations (the tail of the blue curve).

It can be seen that the Jacobi method has constant computational and memory costs per iteration, whereas they are incremental for GMRES without a restart option. The proposed method can be alternatively implemented by using the scalar form in (30), which takes advantage of parallel execution for each sample and avoids storing matrix A'. Since the term $\widetilde{T}_b^{(l-1)}(f(n, p))$ must be recalculated by means of interpolation over the mesh at each iteration, this implementation takes about 220 s per iteration, using six parallel cores on the same machine [the orange curve in Fig. 11(b)].

The impact on memory from the theoretical and vector form of the proposed APC algorithms is similar and, mainly, determined by the size of the (concentrated) system matrix and the boundary condition matrix. For the considered geometry and antenna pattern, at least 5.2 GB of RAM is required to store them in double precision. On the contrary, the implementation of the scalar form of the proposed algorithm is very memory efficient since the system and boundary condition matrices are not precalculated.

V. Conclusion

The scientific objectives of the CIMR mission involve stringent requirements, in terms of both spatial resolution and the required uncertainty on the EO products that determine an upper bound on the measured TOA brightness temperature that cannot exceed 0.5 K. The large deployable mesh reflector of the CIMR antenna guarantees a suitable spatial resolution (<5 km in the Ka-band) but introduces contamination to the measured antenna temperature, which stems from contributions outside the region of interest, i.e., the IFOV or the main beam. In order to meet the radiometric accuracy required, various algorithms for the APC are considered here.

The algorithm has been applied to three synthetic scenarios, chosen as benchmarks due to their geometric discontinuities and radiometric contrast. The comparison between different methods shows that the proposed iterative algorithm, APC-"i," allows fast computation with a performance that depends on the considered spatial benchmark. Considering the uniform

---

[3]The computational burden required to compute the involved matrices is not considered since it can be preliminarily afforded off-line for both algorithms.

[4]Registered trademark.

[5]Trademarked.

main beam, a success rate of 100% is achieved 5–6 km from the discontinuity, whatever the scenario, whereas, in the uniform IFOV case, this happens at 10 km. Therefore, the proposed APC-"i" allows accurate measurements close to the radiometric discontinuities, such as coastlines and ocean sea ice transitions.

The results discussed have been calculated in the Ka-band, but a similar performance (not shown here) has been observed in the K-band. Overall, the results prove that APC goals are achievable with the current antenna design and acquisition strategy; further developments (e.g., the effects of antenna pattern smearing on sample measurements, thermoelastic deformation of the antenna and its impact on antenna pattern, and testing in realistic natural scenarios) will be considered during the next phases of the mission.

APPENDIX A

DERIVATION OF THE FORWARD MODEL

Let $f(n, p)$ be the function that maps $\boldsymbol{r}'[p]$ to the corresponding point in the fixed-to-Earth reference system when the boresight points to $\boldsymbol{r}[n]$. Define $\mathbf{tri}_{f(n,p)}$ as the triangle of the CIMR mesh enclosing the point given by $f(n, p)$ and $\mathbf{tri}_{f(n,p)}[m]$ as the index on the CIMR reference grid corresponding to the mth vertex ($m = 0, 1, 2$) of the triangle $\mathbf{tri}_{f(n,p)}$. Then, the TOA brightness temperature at the point given by $f(n, p)$ is approximated by the following interpolation over the mesh (see Fig. 4):

$$T_b(f(n, p)) = \sum_{m=0}^{2} \boldsymbol{w}'_{(n,p)}[m] \boldsymbol{T_b}\big[\mathbf{tri}_{f(n,p)}[m]\big] \qquad (38)$$

where $\boldsymbol{w}'_{(n,p)}$ is a three-element vector of the barycentric coordinates of the triangle and satisfies

$$\boldsymbol{w}'_{(n,p)}[m] \geq 0 \quad \forall m = 0, 1, 2$$

$$\sum_{m=0}^{2} \boldsymbol{w}'_{(n,p)}[m] = 1. \qquad (39)$$

A general expression for $T_b(f(n, p))$ that encloses both cases for $f(n, p)$, inside and outside the mesh, is

$$T_b(f(n, p)) = \boldsymbol{w}_{(n,p)}^{T} \boldsymbol{T_b} + d(n, p) \qquad (40)$$

where $\boldsymbol{w}_{(n,p)}$ is an N-elements column vector such that its qth entry is given by

$$\boldsymbol{w}_{(n,p)}[q] = \begin{cases} \boldsymbol{w}'_{(n,p)}[m], & \text{if } \exists \, \mathbf{tri}_{f(n,p)} \\ & \wedge \exists \, m : q = \mathbf{tri}_{f(n,p)}[m] \\ 0, & \text{otherwise.} \end{cases} \qquad (41)$$

Also, $d(n, p)$ accounts for the boundary condition

$$d(n, p) = \begin{cases} T_b(f(n, p)), & \text{if } \mathbf{tri}_{f(n,p)} \\ 0, & \text{otherwise.} \end{cases} \qquad (42)$$

By definition, $\boldsymbol{w}_{n,p}$ is an all-zero vector when $f(n, p)$ is outside; on the contrary, $d(n, p)$ is zero when $f(n, p)$ is inside. Moreover, $\boldsymbol{w}_{n,0}[n] = 1$ and zeros for all the remaining positions, whereas $d(n, 0)$ is always zero (both facts follow on from having assumed that $p = 0$ is the index associated with the boresight position).

Substituting (40) into (9) yields

$$\begin{aligned} \boldsymbol{T}_A[n] &= \sum_{p=0}^{P-1} \boldsymbol{c}[p]\big(\boldsymbol{w}_{(n,p)}^{T} \boldsymbol{T_b} + d(n, p)\big) \\ &= \boldsymbol{c}^{T} \begin{bmatrix} \boldsymbol{w}_{(n,0)}^{T} \\ \boldsymbol{w}\boldsymbol{w}_{(n,1)}^{T} \\ \vdots \\ \boldsymbol{w}_{(n,P-1)}^{T} \end{bmatrix} \boldsymbol{T_b} + \begin{bmatrix} d(n, 0) \\ d(n, 1) \\ \vdots \\ d(n, P-1) \end{bmatrix} \boldsymbol{c} \\ &= \boldsymbol{a}_n^{T} \boldsymbol{T_b} + \boldsymbol{d}_n^{T} \boldsymbol{c} \end{aligned} \qquad (43)$$

$\boldsymbol{d}_{(n)} = [d_{(n,0)}, d_{(n,1)}, \ldots, d_{(n,P-1)}]^{T}$ is the vector of boundary conditions and $\boldsymbol{a}_{(n)}$ is defined as

$$\boldsymbol{a}_{(n)} = \big[\boldsymbol{w}_{(n,0)}, \boldsymbol{w}_{(n,1)}, \ldots, \boldsymbol{w}_{n,P-1}\big]\boldsymbol{c}. \qquad (44)$$

Equation (43) represents the sample forward model at n. The vector $\boldsymbol{d}_n$ is an all-zero vector if all the antenna pattern coefficients are inside the mesh. The system forward model is finally written by extending the sample forward model to all boresight positions, yielding (11), where $\boldsymbol{A}$ is the $N \times N$ system matrix

$$\boldsymbol{A} = \big[\boldsymbol{a}_{(0)}, \boldsymbol{a}_{(1)}, \ldots, \boldsymbol{a}_{(N-1)}\big]^{T} \qquad (45)$$

and $\mathbf{D}$ is the $N \times P$ that is the boundary condition matrix

$$\mathbf{D} = \big[\boldsymbol{d}_{(0)}, \boldsymbol{d}_{(1)}, \ldots, \boldsymbol{d}_{(N-1)}\big]^{T} \qquad (46)$$

The vector $\boldsymbol{a}_n$ has four noticeable properties that will be exploited in the following.

The properties of $\boldsymbol{A}$ listed in Section II-C are eventually proved. It should be noted that, by definition, $\boldsymbol{A}[n, m] = \boldsymbol{a}_{(n)}[m]$.

1) $\boldsymbol{a}_{(n)}[m]$ is nonnegative because of the combination of nonnegative quantities (44). This proves (12).

2) Equation (13) follows on from $\boldsymbol{w}_{(n,0)}[n] = 1$ and from the fact that all the other barycentric coordinates are nonnegatives (41).

3) Equation (14) follows from the following relations:

$$\begin{aligned} \sum_{m} |\boldsymbol{A}[n, m]| &= \mathbf{1}^{T}\big[\boldsymbol{w}_{(n,0)}, \boldsymbol{w}_{(n,1)}, \ldots, \boldsymbol{w}_{(n,P-1)}\big]\boldsymbol{c} \\ &\leq \big[\mathbf{1}^{T}\boldsymbol{w}'_{(n,0)}, \mathbf{1}^{T}\boldsymbol{w}'_{(n,0)}, \ldots, \mathbf{1}^{T}\boldsymbol{w}'_{(n,P-1)}\big]\boldsymbol{c} \\ &\leq \mathbf{1}^{T}\boldsymbol{c} \end{aligned} \qquad (47)$$

where $\mathbf{1}$ is the all-ones vector and (44) is used in the second equality; then, we exploited (41) and (39) in the first and second inequalities, respectively. The relation becomes an equality if, and only if, all the antenna pattern coefficients are inside the mesh because it implies that $\mathbf{1}^{T}\boldsymbol{w}_{(n,p)} = \mathbf{1}^{T}\boldsymbol{w}'_{(n,p)} = 1$ from (41) and (39).

4) By substituting $\boldsymbol{c} = \boldsymbol{c_1} + \boldsymbol{c_2}$ into (44) and then into (45), the latter can be rewritten as

$$\boldsymbol{A} = \boldsymbol{A_1} + \boldsymbol{A_2} \qquad (48)$$

where

$$\boldsymbol{A_1} = \big[\boldsymbol{a_{1(0)}}, \boldsymbol{a_{1(1)}}, \ldots, \boldsymbol{a_{1(N-1)}}\big]^{T} \qquad (49)$$

and

$$\boldsymbol{a_{1(n)}} = \big[\boldsymbol{w}_{(n,0)}, \boldsymbol{w}_{(n,1)}, \ldots, \boldsymbol{w}_{n,P-1}\big]\boldsymbol{c_1} \qquad (50)$$
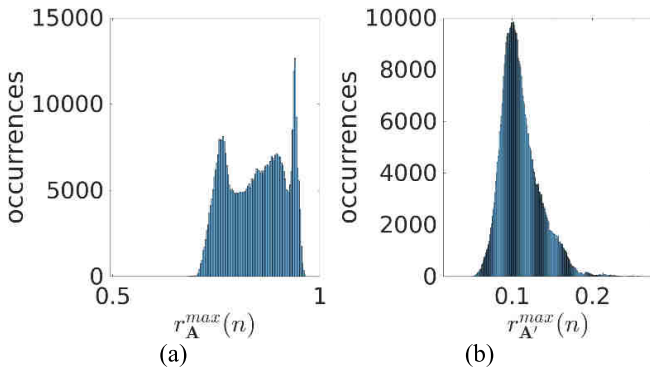
Fig. 12. Empirical distribution of the maximum of the correlation coefficients among the rows, as defined in (52), of (a) system matrix A and (b) concentrated system matrix A' that arises from the proposed APC.

Fig. 13. Ka-band antenna pattern contour levels centered on the nth boresight position over the CIMR mesh (black lines) for a region in the center of the swath. Only the sampling points of the antenna pattern (magenta dots) inside the '$A[n, n]$ region' (red triangles) contribute to the value of $A[n, n]$.

and analogously for A_2. This proves (15).

5) This property follows from the fact that each antenna pattern coefficient is generally associated with three vertices, but the first coefficient is only associated with the boresight position by construction.

APPENDIX B

PROOF OF ZERO-ERROR APC

The zero-error APC can be proved from (7) as follows:

$$
\begin{aligned}
\boldsymbol{e}_{\text{APC}} &= \hat{\boldsymbol{T}}_{A\,\text{ideal}}^{\text{opt}} - \boldsymbol{T}_{A\,\text{ideal}} \\
&= A_{\text{ideal}} A^{\dagger}(\boldsymbol{T}_A - \mathbf{D}\boldsymbol{c}) + \boldsymbol{d}_{\text{ideal}} - A_{\text{ideal}}\boldsymbol{T}_b - \boldsymbol{d}_{\text{ideal}} \\
&= A_{\text{ideal}} A^{\dagger}(\boldsymbol{T}_A - \mathbf{D}\boldsymbol{c}) - A_{\text{ideal}}\boldsymbol{T}_b \\
&= A_{\text{ideal}} A^{\dagger}(A\boldsymbol{T}_b + \mathbf{D}\boldsymbol{c} - \mathbf{D}\boldsymbol{c}) - A_{\text{ideal}}\boldsymbol{T}_b \\
&= A_{\text{ideal}} A^{\dagger}A\boldsymbol{T}_b - A_{\text{ideal}}\boldsymbol{T}_b \\
&= A_{\text{ideal}}\big(\mathbf{I} - \text{null}(A)\text{null}(A)^T\big)\boldsymbol{T}_b - A_{\text{ideal}}\boldsymbol{T}_b \\
&= A_{\text{ideal}}\boldsymbol{T}_b - A_{\text{ideal}}\text{null}(A)\text{null}(A)^T\boldsymbol{T}_b - A_{\text{ideal}}\boldsymbol{T}_b \\
&= 0 \qquad\qquad\qquad\qquad\qquad\qquad\qquad (51)
\end{aligned}
$$

where (17) and (18) have been substituted in the second step and (11) has been substituted in the fourth step. The identity $A^{\dagger}A = \mathbf{I} - \text{null}(A)\text{null}(A)^T$, where $\mathbf{I}$ is the identity matrix, has been used in the sixth step and the identity $A_{\text{ideal}}\text{null}(A) = \mathbf{0}$, which follows from the hypothesis that $\text{null}(A) \subseteq \text{null}(A_{\text{ideal}})$, is substituted in the last step.

APPENDIX C

RELATION BETWEEN ANTENNA PATTERN AND ALGORITHM CONVERGENCE

It is first shown that the system matrix is badly conditioned. Let us define $r_A^{\max}(n)$ as the maximum of the correlation coefficient between the nth row of A and the remaining ones, i.e.,

$$
r_A^{\max}(n) = \frac{r_A(n, n')}{\sqrt{r_A(n, n)r_A(n', n')}} \qquad (52)
$$

where $r_A(n, n') \sum_{m=0}^{N-1} A[n, m]A[n', m]$. Fig. 12(a) reports the empirical distribution of $r_A^{\max}(n)$ for the system matrix of the simulations in the Ka-band reported in Section IV.

The minimum, average, and maximum values of $r_A^{\max}(n)$ are 0.52, 0.84, and 0.98, respectively. The high correlation among the rows and their number ($N \approx 4.72 \times 10^5$ in the Ka-band
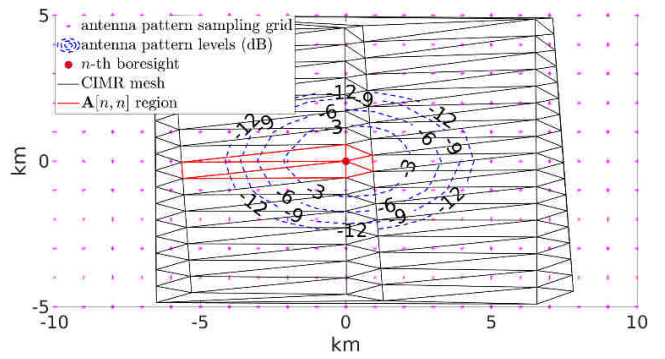
for a region of size 500×1500 km in the central part of the swath) makes the system matrix numerically hard to invert. On the contrary, the corresponding concentrated system matrix exhibits a low correlation [Fig. 12(b)] and it is numerically stable for inversion.

Therefore, the computation of A^{-1} is very resource-demanding and prone to finite-arithmetic issues. A partial solution that foresees the computation of A^{-1} with a low-rank approximation would be computationally heavy and A^{-1} should be recomputed each time that the CIMR reference grid or the orbital parameters change.

It can be verified, through (27), that A does not satisfy the necessary sufficient condition for convergence and, therefore, it is not strictly diagonally dominant. In the following, the correlation between this fact and the characteristics of the antenna pattern is explored.

According to (44), the coefficients on the main diagonal $A[n, n]$ are given by

$$
A[n, n] = \big[\boldsymbol{w}_{(n,0)}[n], \boldsymbol{w}_{(n,1)}[n], \ldots, \boldsymbol{w}_{(n,P-1)}[n]\big]\boldsymbol{c} \qquad (53)
$$

In practical terms, $A[n, n]$ is the sum of the coefficients of the antenna pattern centered in $\boldsymbol{r}[n]$, weighted by their barycentric coordinates with respect to the position $\boldsymbol{r}[n]$. The sketch in Fig. 13 depicts the reciprocal position of the Ka-band antenna pattern and the CIMR reference grid during the acquisition of sample n in a central region of the swath. For a given antenna pattern sampling grid (magenta points), only the coefficients associated with the points inside the $A[n, n]$-region (red triangles) contribute to the value of $A[n, n]$. The plots in Fig. 14 show the value of $A[n, n]$ in the scenario of Fig. 13, as a function of the density of antenna pattern sampling grid, assuming the overall gain $C = 1$.

As the sampling becomes denser ($P \to +\infty$), $A[n, n]$ converges to the integral of the antenna pattern over the $A[n, n]$-region

$$
\begin{aligned}
A[n, n] &= \iint_{A[n,n]\text{region}} A_n(\boldsymbol{r})w(n, \boldsymbol{r})d\boldsymbol{r} \\
&\leq \iint_{A[n,n]\text{region}} A_n(\boldsymbol{r})d\boldsymbol{r} \qquad (54)
\end{aligned}
$$

where $w(n, \boldsymbol{r})$, $w(n, \boldsymbol{r}) \leq 1$ is the barycentric coordinate with respect to position $\boldsymbol{r}[n]$. The value of c_0, and those of the gain of the antenna pattern inside the $A[n, n]$-region, is also reported for comparison. This example shows that
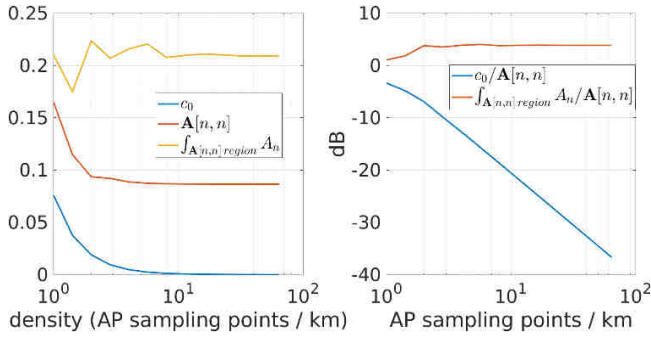
Fig. 14. Comparison among c_0, $A[n,n]$ and the overall gain inside the $A[n,n]$ region, for the scenario in Fig. 13 and for increasing density of the antenna pattern sampling grid: (Left) linear values and (Right) normalized with respect to $A[n,n]$.
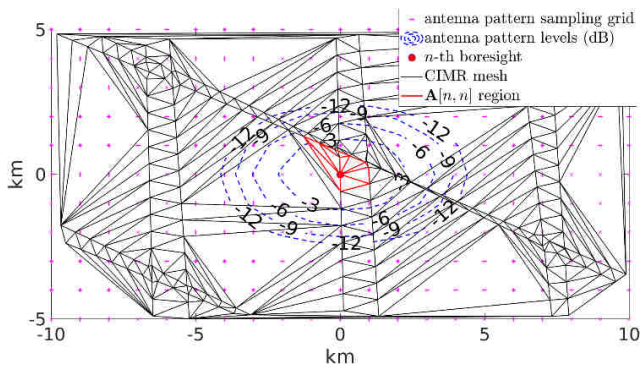

Fig. 15. Ka-band antenna pattern contour levels centered on the nth boresight position over the CIMR mesh (black lines) for a region in the peripheral swath. Only the sampling points of the antenna pattern (magenta dots) inside the "$A[n,n]$ region" (red triangles) contribute to the value of $A[n,n]$.
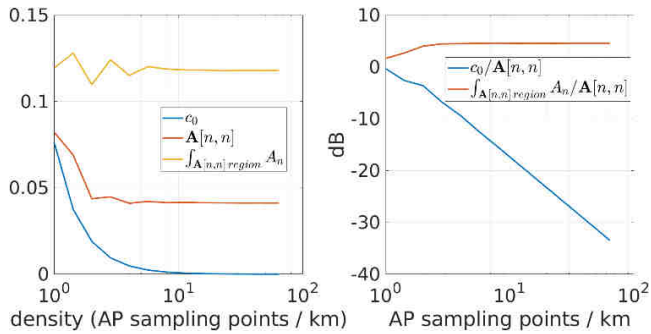

Fig. 16. Comparison among c_0, $A[n,n]$, and the overall gain inside the $A[n,n]$ region for the scenario in Fig. 15 and for increasing density of the antenna pattern reference grid: (Left) linear values and (Right) normalized with respect to $A[n,n]$.

the system matrix A is not strictly diagonally dominant because the $A[n,n]$ coefficient is lower than $C/2$. For the sake of completeness, a scenario related to the acquisition in a peripheral region of the swath is shown in Fig. 15. The values of the antenna pattern gain, shown in Fig. 16, are lower than in the previous scenario because the $A[n,n]$-region is narrower.

The inequality in (54) states that a necessary condition for the system matrix to be strictly diagonally dominant is that the gain in the $A[n,n]$-region is greater than $C/2$ for all n.

Figs. 14 and 15 show that an extremely high antenna directivity is required, in practice; by using the concentrated

system matrix, we mathematically enforce this condition by construction at the price of a mismatch error. In other terms, the mismatch error is the tradeoff between the proposed fast and computationally feasible APC algorithm and a real antenna, whose directivity is not sufficient for the resolution of the CIMR reference grid.

APPENDIX D
PROOF OF CONVERGENCE

A' is proven to be strictly diagonally dominant, which means that it fulfills (28) as follows:

$$
\begin{aligned}
\left| A'[n,n] \right| &- \sum_{m \neq n} \left| A'[n,m] \right| \\
&= a'_{(n)}[n] - \left(\mathbf{1}^T a'_{(n)} - a'_{(n)}[n] \right) \\
&= 2a'_{(n)}[n] - \mathbf{1}^T a'_{(n)} \\
&\geq 2c'[0] - \mathbf{1}^T a'_{(n)} \\
&\geq 2c_{\text{FOCUS}} - \mathbf{1}^T a'_{(n)} \\
&> C - \mathbf{1}^T a' \\
&> C - \mathbf{1}^T c' > 0
\end{aligned}
\tag{55}
$$

where the absolute values can be dropped from (12) and the first equality follows from (44). The first inequality follows from (13), the second inequality follows from (21), the third inequality follows from (20), the fourth inequality follows from (14), and the last inequality follows from (8b). The relation holds for all n; thus, A' is strictly diagonally dominant.

REFERENCES

[1] H. O. Portner, D. C. Roberts, and V. Masson-Delmotte, *The Ocean and Cryosphere in a Changing Climate: Special Report of the Intergovernmental Panel on Climate Change*, 1st ed. Cambridge, U.K.: Cambridge Univ. Press, 2022, doi: 10.1017/9781009157964.

[2] European Commission, Copernicus Evolution LC-SPACE-02-EO-2018 LC-SPACE-03-EO-2018, *Guidance Document for Horizon 2020 Work Programme 2018–2020*, Oct. 2017.

[3] W. N. Meier, T. Markus, and J. J. Comiso, "AMSR-E/AMSR2 unified L3 daily 12.5 km brightness temperatures, sea ice concentration, motion & snow depth polar grids, version 1," NASA Nat. Snow Ice Data Center Distrib. Act. Arch. Center, 2018. [Online]. Available: https://nsidc.org/data/au_si12/versions/1, doi: 10.5067/RA1MIJOYPK3P.

[4] Earth and Mission Science Division, *Copernicus Imaging Microwave Radiometer (CIMR) Mission Requirements Document*, European Space Agency, Noordwijk, The, Netherlands, Oct. 2020. [Online]. Available: https://esamultimedia.esa.int/docs/EarthObservation/CIMR-MRD-v4.0-20201006_Issued.pdf

[5] M. Brogioni et al., "Preliminary studies on CIMR antenna pattern brightness temperature compensation," *IEEE J. Sel. Top. Appl. Earth Observ. Remote Sens.*, vol. 15, pp. 173–183, 2022, doi: 10.1109/JSTARS.2021.3124829.

[6] D. M. Le Vine, G. S. E. Lagerloef, and S. E. Torrusio, "Aquarius and remote sensing of sea surface salinity from space," *Proc. IEEE*, vol. 98, no. 5, pp. 688–703, May 2010, doi: 10.1109/JPROC.2010.2040550.

[7] T. Meissner, F. Wentz, and D. Draper, "GMI calibration algorithm and analysis theoretical basis document," Remote Sensing Systems, Santa Rosa, CA, USA, Version G, Tech. Rep. 041912, 2012, doi: 10.56236/RSS-au.

[8] P. W. Gaiser et al., "The WindSat spaceborne polarimetric microwave radiometer: Sensor description and early orbit performance," *IEEE Trans. Geosci. Remote Sens.*, vol. 42, no. 11, pp. 2347–2361, Nov. 2004, doi: 10.1109/TGRS.2004.836867.

[9] J. Peng et al., "Soil moisture active/passive (SMAP) L-band microwave radiometer post-launch calibration upgrade," *IEEE J. Sel. Topics Appl. Earth Observ. Remote Sens.*, vol. 12, no. 6, pp. 1647–1657, Jun. 2019, doi: 10.1109/JSTARS.2019.2902492.

[10] R. C. Gonzalez and R. E. Woods, *Digital Image Processing*, 3rd ed. Upper Saddle River, NJ, USA: Prentice-Hall, 2008.

[11] V. González-Gambau, A. Turiel, E. Olmedo, J. Martínez, I. Corbella, and A. Camps, "Nodal sampling: A new image reconstruction algorithm for SMOS," *IEEE Trans. Geosci. Remote Sens.*, vol. 54, no. 4, pp. 2314–2328, Apr. 2016, doi: 10.1109/TGRS.2015.2499324.

[12] D.-T. Lee and B. J. Schachter, "Two algorithms for constructing a Delaunay triangulation," *Int. J. Comput. Inf. Sci.*, vol. 9, no. 3, pp. 219–242, 1980, doi: 10.1007/BF00977785.

[13] Y. Saad, *Iterative Methods for Sparse Linear Systems*, 2nd ed. Philadelphia, PA, USA: SIAM, 2003, doi: 10.1137/1.9780898718003.

Alessandro Lapini received the M.Sc. degree (summa cum laude) in telecommunications engineering and the Ph.D. degree in computer science, systems and telecommunications from the University of Florence, Florence, Italy, in 2010 and 2014, respectively.

Since 2014, he has been a Research Assistant with the University of Florence, where he has been initially with the Department of Information Engineering and then with the Department of Industrial Engineering since 2015. From 2016 to 2018, he was a Research Fellow with the Department of Industrial Engineering. University of Florence. Since 2019, he has been with the Microwave Remote Sensing Group, Institute of Applied Physics Nello Carrara (IFAC), Consiglio Nazionale delle Ricerche (CNR), Florence. His research interests are mainly focused on signal and image processing, particularly in the field of remote sensing and biomedical imaging, acoustics, and active noise control.

Ada Vittoria Bosisio (Member, IEEE) received the M.S. degree in electronic engineering and the Ph.D. degree in applied electromagnetism from the Politecnico di Milano, Milan, Italy, in 1991 and 1995, respectively.

During her Ph.D. degree, she was involved in the Olympus and Italsat propagation experiments for the aspects related to propagation-oriented radiometry (Ka-band). From 1995 to 1997, she was a Research Associate with the CETP/CNRS Laboratory, Vélizy-Villacoublay, France, where she has been active in measurements and analysis of forest attenuation and scattering at 2 and 6 GHz. From 1997 to 1998, she was with CNET/France Telecom, Issy-les-Moulineaux, France, as an Ingenieur de Recherche, working on radio-wave effects induced by GSM on the environment and on individuals. From 1999 to 2001, she was with the Propagation Group, Politecnico di Milano, as a Research Associate working on satellite links at low elevation angle in the K- and W-bands and on propagation of TV broadcast and digital radio links over mountains through ray techniques. Since 2001, she has been a Researcher with the IEIIT Institute, Italian National Research Council, Milan, working on remote sensing applications related to atmospheric science and tropospheric propagation. Her research interests include microwave radiometry and the interaction mechanisms between signal and complex media in the terrestrial biosphere.

Giovanni Macelloni (Senior Member, IEEE) received the M.Sc. degree in electronic engineering from the University of Florence, Florence, Italy, in 1993.

Since 1995, he has been working at the Institute of Applied Physics-CNR, Florence, where is currently the Head of Research. Since 2019, he has been an Adjunct Professor with the University of Venice, Venice, Italy. He is a member of the Cryonet team of Global Cryosphere Watch of the WMO and the Italian Scientific Antarctic Commission, which implements the national Antarctic program. He has worked as a tutor for Ph.D. students. His research has been carried out in the framework of several national and international programs granted by Italian Entities, the European community, and Space Agencies (ESA, ASI, NASA, and JAXA) and includes the participation in international teams for the studying of the cryosphere and the development and assessment of future spaceborne missions. His research interests include microwave active and passive remote sensing for the study of the Earth system and cryosphere in particular. He is also involved in the design and development of microwave remote sensing systems both from the ground, the air, and satellites.

Mr. Macelloni served as a reviewer for several international committees, organizations, and international journals, and acted as an organizer and the co-chair of international conferences. He is an Associate Editor of IEEE TRANSACTIONS ON GEOSCIENCE AND REMOTE SENSING.

Marco Brogioni (Member, IEEE) was born in Siena, Italy, in 1976. He received the M.Sc. degree in telecommunications engineering from the University of Siena, Siena, in 2003, and the Ph.D. degree in remote sensing from the University of Pisa, Pisa, Italy, in 2008.

Since 2004, he has been with the Microwave Remote Sensing Group, Institute of Applied Physics Nello Carrara (IFAC), Consiglio Nazionale delle Ricerche (CNR), Florence, Italy. From 2006 to 2007, he was a Visiting Student at the University of California at Santa Barbara, Santa Barbara, CA, USA. He participated in the Italian Antarctic Expeditions, carrying out his research at Concordia Station (Dome-C) and Mario Zucchelli Station (Ross Sea) in 2013, 2015, and 2018. His research interests include passive and active microwave remote sensing applied to snow by using satellite and ground-based data, especially regarding the development of electromagnetic models for passive and active microwave remote sensing of snow, vegetation, and soil. He is also involved in the design and manufacturing of microwave radiometers (L- to Ka-bands). He is currently involved in several international projects regarding polar regions.

Dr. Brogioni was a recipient of the Third Prize at the URSI GA Student Prize Paper Competition in Chicago, IL, USA, in 2008. He served as the Chair for the 16th MicroRad 2020 virtual meeting and in the Local Organizing Committee of the 10th Microrad, Florence, in 2008, and the Microwave Signature Symposium of the URSI Commission-F, Florence, in 2010.